

# Masses and activity of AB Doradus B a/b<sup>★</sup>

## The age of the AB Dor quadruple system revisited

U. Wolter<sup>1</sup>, S. Czesla<sup>1</sup>, B. Fuhrmeister<sup>1</sup>, J. Robrade<sup>1</sup>, D. Engels<sup>1</sup>, M. Wieringa<sup>2</sup>, and J. H. M. M. Schmitt<sup>1</sup>

<sup>1</sup> Hamburger Sternwarte, University of Hamburg, Gojenbergsweg 112, 21029 Hamburg, Germany  
e-mail: uwolter@hs.uni-hamburg.de

<sup>2</sup> CSIRO, ATNF, Locked Bag 194, NSW 2390 Narrabri, Australia

Received 5 May 2014 / Accepted 13 August 2014

### ABSTRACT

We present a multiwavelength study of the close binary AB Dor Ba/b (Rst137B). Our study comprises astrometric orbit measurements, optical spectroscopy, X-ray and radio observations. Using all available adaptive optics images of AB Dor B taken with VLT/NACO from 2004 to 2009, we tightly constrain its orbital period to  $360.6 \pm 1.5$  days. We present the first orbital solution of Rst 137B and estimate the combined mass of AB Dor Ba+b as  $0.69^{+0.02}_{-0.24} M_{\odot}$ , slightly exceeding previous estimates based on IR photometry. Our determined orbital inclination of Rst 137B is close to the axial inclination of AB Dor A inferred from Doppler imaging. Our VLT/UVES spectra yield high rotational velocities of  $\geq 30 \text{ km s}^{-1}$  for both components Ba and Bb, in accord with previous measurements, which corresponds to rotation periods significantly shorter than one day. Our combined spectral model, using PHOENIX spectra, yields an effective temperature of  $3310 \pm 50 \text{ K}$  for the primary and approximately 60 K less for the secondary. The optical spectra presumably cover a chromospheric flare and show that at least one component of Rst 137B is significantly active. Activity and weak variations are also found in our simultaneous *XMM-Newton* observations, while our ATCA radio data yield constant fluxes at the level of previous measurements. Using evolutionary models, our newly determined stellar parameters confirm that the age of Rst 137B is between 50 and 100 Myr.

**Key words.** stars: activity – stars: coronae – stars: low-mass – stars: rotation – binaries: general – stars: individual: Rst 137B

## 1. Introduction

AB Dor A is one of the closest, brightest, and most intensively studied highly active stars, see, e.g., [Cohen et al. \(2010\)](#) for an extensive list of references. In November 2009 we performed a multiwavelength study of the AB Dor system. While the results for AB Dor A are presented in [Lalitha et al. \(2013\)](#), in this paper we report our findings on AB Dor B (=Rst 137B).

### 1.1. The AB Dor quadruple system

AB Dor A was first detected as a rotationally variable star by [Pakull \(1981\)](#) who furthermore identified it with a strong X-ray source detected by the *Einstein* satellite. In contrast to its original classification as a RS CVn star, AB Dor A was later found to be neither evolved nor accompanied by a close, massive companion. Instead, AB Dor A is a fast-rotating dwarf star of spectral type  $\approx \text{K1V}$  close to or on the early main sequence ([Wichmann et al. 1998](#)). Because of its intense activity and relative proximity ( $15.17 \pm 0.13 \text{ pc}$ , [van Leeuwen 2007](#)), AB Dor A plays an important role for the study of stellar coronae (e.g., [Güdel 2004](#), and references there).

AB Dor A's visual companion AB Dor B (=Rst 137B), about  $9.5''$  away from AB Dor A and considerably fainter ( $V = 12.6 \pm 0.2 \text{ mag}$ , [Collier Cameron & Foing 1997](#)) was confirmed as a physical companion by radial velocity and astrometric measurements ([Martin & Brandner 1995](#), and references therein). While the activity of Rst 137B was noticed early on in the *Einstein* X-ray data of 1979 ([Vilhu & Linsky 1987](#)), its own binarity was only detected after the advent of adaptive optics. As a side-product of the detection of AB Dor C, [Close et al. \(2005\)](#) resolved Rst 137B with a separation of about  $0.7''$  between its components Rst 137Ba and Rst 137Bb, which were later confirmed by [Janson et al. \(2007\)](#) as two M dwarf stars. [Close et al. \(2007\)](#) give spectral types of  $\text{M}3.5 \pm 1.5$  and  $\text{M}4.5 \pm 1.5$  for the two components without further reference. [Guirado et al. \(2006\)](#) report an upper limit to the mass of Rst 137B of 0.4 solar masses, based on the astrometric sampling of its orbit around AB Dor A. However, the uncertainties of this dynamical estimate are large because of the sparse sampling of the orbit, which appears to have a period  $\geq 1000a$  (see, e.g., Fig. 4 of [Guirado et al. 2006](#)).

Finally, AB Dor C was found at a distance of about  $0.16''$  from AB Dor A, see, e.g., [Boccaletti et al. \(2008\)](#). It orbits AB Dor A with a period of 11.7 years and a semimajor axis of approximately 5 AU ([Nielsen et al. 2005](#)). The original dynamical mass estimate of  $0.08$  to  $0.11 M_{\odot}$  ([Guirado et al. 1997](#)) was later constrained to  $0.090 \pm 0.005 M_{\text{Sun}}$  ([Close et al. 2007](#)), which places it close to, but safely above, the brown dwarf limit. Nevertheless, because of its well-constrained dynamical mass, AB Dor C is one of a few key objects for testing or calibrating low-mass evolutionary models ([Luhman 2012](#)).

<sup>★</sup> Based on observations collected at the European Southern Observatory, Paranal, Chile, 383.D-1002(A) and the ESO Science Archive Facility. Using data obtained with *XMM-Newton*, an ESA science mission with instruments and contributions directly funded by ESA Member states and NASA. Using data obtained with the Australia Telescope Compact Array (ATCA) operated by the Commonwealth Scientific and Industrial Research Organisation (CSIRO).

### 1.2. The age of the AB Dor system

Age estimates of the AB Dor system range between 30 and 150 Myr (Collier Cameron & Foing 1997; Luhman et al. 2005; Janson et al. 2007; Guirado et al. 2011). The system age is of particular interest for understanding the evolutionary status of the very low mass star AB Dor C, as well as in the context of the age of the AB Dor moving group, see Reipurth (2008).

Luhman et al. (2005) use color-magnitude diagrams to compare the AB Dor moving group with the Pleiades and IC 2391. They conclude that (a) a conservative age estimate for the AB Dor system and moving group is 75–150 Myr. Furthermore, they estimate (b) that Rst 137B is “clearly not younger than the Pleiades” ( $\tau = 130 \pm 20$  Myr, Barrado y Navascués et al. 2004; Soderblom et al. 2009) and suggest (c) that the AB Dor moving group, as judged by similar space velocity vectors, could stem from a star formation event that also formed the Pleiades.

Partly contradicting Luhman et al., Janson et al. (2007) use evolution models of Baraffe et al. (1998) and comparisons with the above named clusters to infer an age range of 50–100 Myr, which is several 10 Myr younger than the value at item (a) above and presumably younger than the Pleiades. In this context it is important that Janson et al. doubt the validity of item (c) above. They argue that the space positions combined with the space velocities of the AB Dor moving group exclude their common origin with the Pleiades in the same region. Finally, based on an analysis of galactic dynamics, Ortega et al. (2007) again support the proposal of Luhman et al. of a common origin of the Pleiades and the AB Dor moving group, estimating its age to be  $119 \pm 20$  Myr.

AB Dor A itself is only poorly suited for a reliable age determination because of its extreme activity. Guirado et al. (2011) estimate AB Dor A’s age to be between 40 and 50 Myr, based on its well-known stellar parameters, see their Table 2. However, they remark that the strong magnetic fields and fast rotation of AB Dor A, as yet largely unaccounted for, could significantly influence that estimate. Furthermore, they state that “older ages are not completely excluded” by their data. In addition, AB Dor C is currently not suited to determine the system age because of its low mass. Its original age estimate of 65 Myr (Close et al. 2005) has been a matter of intense discussion ever since, see, e.g., Guirado et al. (2011) and references there.

As already noted in earlier studies, Rst 137B plays an important role for age-dating the system: While Pakull (1981) suggested to use it to test the now obsolete post-main-sequence hypothesis for AB Dor A, Rucinski (1985) proposed that it could be used to confine the then unknown distance of the AB Dor system. Today, along the lines of Pakull’s argument, its importance lies in its moderately low mass, which makes an age estimate close to the main sequence more sensitive than for AB Dor A (see, e.g., Fig. 1 of Luhman et al. 2005).

### 1.3. Radio observations of Rst 137B

White et al. (1988) located the main radio emission from AB Dor at the position of AB Dor A with a precision of  $\approx 1''$ . Lim (1993), based on observations between July and November 1990, detected radio emission from Rst 137B, which they describe as (a) typically an order of magnitude weaker than that of AB Dor A and (b) normally “approximately constant ... at approximately 2 mJy” (at 6 cm wavelength, more precisely, a frequency of 4790 MHz). Lim furthermore finds that during “impulsive flares” Rst 137B reaches 4 mJy in that band with a high degree of polarization. Later, Lim et al. (1994) analyze observations from

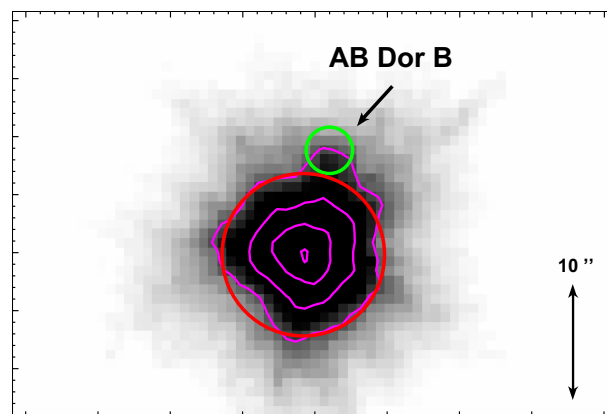


**Fig. 1.** X-ray image of AB Dor taken on 2009 November 25 and 26 with *XMM-Newton*’s MOS1 camera with a total exposure time of 58 ksec. Clearly, AB Dor A and Rst 137B are only moderately resolved by *XMM-Newton*. The red and green circles show our extraction regions used for AB Dor A and Rst 137B. Brightness scaling is linear, contour levels are plotted at 300, 600, 1600, and 2400 counts/bin.

December 1990 to January 1991, and still detect Rst 137B as a “steady (quiescent) source”. We summarize that Rst 137B has hitherto been observed as a steady source with a typical flux density of 2 mJy at about 5 GHz with flares reaching twice that value.

### 1.4. AB Dor in X-rays

AB Dor is among the brightest coronal X-ray sources in the sky, and the system has been extensively studied, mostly focussing on the primary AB Dor A, which dominates the X-ray emission of the system (e.g., Kuerster et al. 1997; Güdel et al. 2001; Sanz-Forcada et al. 2003; García-Alvarez et al. 2008; Lalitha et al. 2013). While the components of Rst 137B cannot be separated by any current or past X-ray telescope, already Vilhu & Linsky (1987) derived an X-ray flux for Rst 137B as a whole of  $F_X = 1 \pm 0.1 \times 10^{-12}$  erg cm $^{-2}$  s $^{-1}$  for the 0.2–4.0 keV energy band. Given its distance of 15.17 pc and a small correction factor negligible here, this corresponds to an X-ray luminosity of  $L_X = 2.8 \times 10^{28}$  erg s $^{-1}$  in the 0.2–5.0 keV band. Sanz-Forcada et al. (2003) reported asymmetries in *XMM* images of AB Dor, which can be clearly attributed to Rst 137B as deduced from fully resolved *Chandra* images. From an analysis of the *Chandra* zeroth-order ACIS-S spectrum obtained in 1999 they report  $F_X = 1.3 \times 10^{-12}$  erg cm $^{-2}$  s $^{-1}$  in the 6–25 Å band ( $\approx 0.5$ –2.0 keV), which translates into about  $5.2 \times 10^{28}$  erg s $^{-1}$  in the 0.2–5.0 keV band, that is, without a pronounced change compared with the measurements about 20 years earlier. García-Alvarez et al. (2008) present a detailed analysis of the high-resolution HETGS spectrum of Rst 137B from the 1999 *Chandra* observation. They determine a differential emission measure (DEM) with a broad distribution and a peak at about 10 MK as well as an abundance pattern (IFIP) that is typical for active stars.

## 2. Observation and data analysis

On 25 and 26 November 2009 we simultaneously obtained multiwavelength data of AB Dor A and Rst 137B using *XMM-Newton* (observation Id 0602240201), UVES mounted on

the VLT Kueyen telescope, and the Australian Compact Array (ATCA), see [Lalitha et al. \(2013\)](#) for results and details concerning AB Dor A. Furthermore, our analysis makes use of archival data: adaptive optics images from the VLT/NACO. The corresponding program IDs are given in [Table 1](#).

### 2.1. Optical spectra

UVES was operated in dichroic mode, leading to a spectral coverage from 3720 Å to 4945 Å and 5695 Å to 9465 Å with another small gap from 7532 Å to 7655 Å falling onto the gap between the CCDs of the red spectrograph arm. We used exposure times of 300 s and 200 s, the spectral resolution of our spectra is  $\sim 40\,000$  for the blue and 60 000 for the red arm spectra. The spectra were reduced and flux calibrated using the UVES pipeline version 4.4.8 ([Ballester et al. 2000](#)).

We observed two pairs of spectra, which we number for future reference: spectrum 1 on 26 November 2009 at UT 01:56, spectrum 2 at UT 02:03, spectrum 3 at UT 08:20, and spectrum 4 at UT 08:24.

### 2.2. VLT/NACO adaptive optics images

AB Dor A and Rst 137B have been the target of several observing campaigns using the NAOS adaptive optics system and the CONICA near-infrared camera mounted on UT 4 of the ESO VLT ([Lenzen et al. 2003](#); [Rousset et al. 2003](#)). These campaigns cover the time span 2004 to 2009. We retrieved all frames covering Rst 137B from the ESO archive. For consistency we used exposures with the *Ks* filter, centered on 2.18  $\mu\text{m}$ , with a full width at half maximum (FWHM) of 0.35  $\mu\text{m}$ . When this filter had not been used, we alternatively also accepted the NB 2.17 filter, centered on 2.166  $\mu\text{m}$ , with a FWHM of 0.023  $\mu\text{m}$  (i.e., on the  $\gamma$  line of the hydrogen bracket series).

We used the NACO pipeline supplied by ESO to reduce the raw frames (version 4.3.2, Common Pipeline Library CPL 5.3.1). The reduction steps were (1) a correction by a master lamp flat-field built for each observing date; and (2) a combination of the dithering exposures for each set. For step (1) we used lamp flats, since sky flats were usually not available. According to the NACO pipeline manual, they agree with sky flats to “within 5%”. Step (2) includes a subtraction of the sky background, as estimated by the pipeline procedure “naco\_img\_jitter”.

The resulting combined images are summarized in [Table 1](#), where the listed times refer to the start time of the first exposure of each set. Since each set covers about half an hour, the individual image times are irrelevant for our analysis. Fortunately, some of the exposures on 2005 January 7, although aimed at AB Dor A, also covered Rst 137B, albeit with an incomplete dithering pattern.

### 2.3. XMM-Newton X-ray data

AB Dor was observed by *XMM-Newton* from 25 November 2009 20:54 UT to 26 November 13:08 UT. With a separation of about 9 arcsec, AB Dor A and Rst 137B are only moderately resolved by *XMM-Newton* whose point spread function (PSF) has a FWHM of about 6”. However, as discussed below, the main problem of extracting the signal of Rst 137B from the XMM-images is its high contrast relative to AB Dor A in combination with slightly irregular “spikes” of the PSF. The situation is illustrated in [Fig. 1](#), which shows our X-ray image of

**Table 1.** VLT/NACO exposures.

Date and UT time	Program	Filter	Number of exposures
2004-02-03 01:52	60.A-9026	NB 2.17	18
2005-01-07 05:08	074.C-0084	<i>Ks</i>	4
2005-11-28 02:07	076.C-0339	<i>Ks</i>	15
2008-08-25 09:16	381.C-0096	<i>Ks</i>	17
2008-11-08 07:56	382.C-0058	<i>Ks</i>	17
2008-12-19 03:09	382.C-0058	<i>Ks</i>	17
2009-01-01 03:55	382.C-0058	<i>Ks</i>	23
2009-02-17 01:35	382.C-0058	<i>Ks</i>	17

the AB Dor system obtained in 2009 with the MOS1 camera of the EPIC instrument (Metal-Oxide-Silicon, European Photon Imaging Camera) of *XMM-Newton*<sup>1</sup>. The MOS1 camera is best suited for our analysis since it has a well-sampled, largely circular PSF. Hence, we exclusively used MOS1 data to study Rst 137B; MOS1 was operated with the medium filter inserted.

Because AB Dor is an *XMM-Newton* calibration target, it has regularly been observed since the beginning of the mission; we analyzed several of these data sets for comparison with the 2009 observation. All data were reduced with the *XMM-Newton* Science Analysis System software SAS 10.0 and standard SAS tools were used to produce images, light curves, and spectra ([de la Calle 2012](#)). The extreme X-ray brightness of AB Dor A, about a factor of 20–50 brighter than Rst 137B, results in significant contamination of the X-ray signal at the position of Rst 137B. In contrast, *Chandra* resolves the components, and we clearly locate Rst 137B at a separation of 9.2 arcsec and a position angle of 255 deg in the ACIS image. The relative positions do not change significantly over a decade (see, e.g., [Guirado et al. 2006](#)), and we used a corresponding region-template centered on AB Dor A in the MOS1 images. Source photons for Rst 137B were extracted in the 0.2–3.0 keV energy range from the 2 arcsec radius circular region shown in [Fig. 1](#). In addition, we used two suitably chosen control regions of identical size and separation from AB Dor A to determine the background and contamination at the position of Rst 137B. About 30 to 40% of the signal in the source region are expected to originate from Rst 137B.

### 2.4. ATCA radio data

We obtained data of AB Dor A and Rst 137B with the Australia Telescope Compact Array (ATCA) from 25 November 2009 19:25 UT to 26 November 18:00 UT with a gap between 0:05 UT and 6:30 UT on 26 November. Unfortunately, the flare we observed in the optical chromospheric lines, discussed in [Sect. 4.3](#), falls into that gap. The observations simultaneously covered the 5.5 GHz (5.5 cm) and 9 GHz (3.3 cm) bands with a bandwidth of 2 GHz each, using 10 s integrations, which we rebinned to 30 s for the final light curves. The array was in configuration 6B with baselines reaching 6000 m, providing a spatial resolution up to 1 arcsec at the observed frequencies, which means that AB Dor A and Rst 137B are clearly separated. See [Lalitha et al. \(2013\)](#) for details of the reduction and calibration procedures.

<sup>1</sup> See the *XMM-Newton* Users Handbook at <http://xmm.esac.esa.int> for a detailed description of the instrument.

**Table 2.** Relative position and flux ratio of Rst 137Bb with respect to Rst 137Ba for the NACO images listed in Table 1.

Date	Distance		Pos. angle [degree]	Flux ratio
	[pix]	[mas]		
2004.0905	4.88	64.8	241.2	0.81
2005.0191	5.29	70.2	247.0	0.75
2005.9085	5.03	66.8	266.6	0.64
2008.6499	1.43	19.0	149.5	2.13
2008.8551	4.68	62.1	260.8	0.78
2008.9668	4.99	66.3	248.0	0.75
2009.0025	4.76	63.2	245.0	0.77
2009.1309	4.22	56.1	234.3	0.74

**Notes.** The distance at 2008.6499 is only an upper bound. The uncertainty of the distance measurements is about  $\pm 3.0$  mas ( $1\sigma$ ).

### 3. Astrometric orbit and the system mass

#### 3.1. Analyzing the VLT/NACO images

To each NACO image of Rst 137B listed in Table 1 we fitted a function of the CCD columns  $x$  and rows  $y$  of the form

$$f(x, y) = a_0 + a_1 e^{-u/2} + a_5 e^{-v/2} \quad (1)$$

$$\text{with } u = ((x - a_3)/a_2)^2 + ((y - a_4)/a_2)^2$$

$$\text{and } v = ((x - a_6)/a_2)^2 + ((y - a_7)/a_2)^2,$$

that is, the sum of a pair of 2D Gaussians with common width,  $a_2$ , on a background given by  $a_0$ . Using a Levenberg-Marquart optimizer as supplied by the IDL routine CURVEFIT, we fitted the center coordinates of the two Gaussians,  $(a_3, a_4)$  and  $(a_6, a_7)$ , and computed the distances and position angles given in Table 2. To translate CCD into sky positions, we used the scale of 0.01327 arcsec per pixel given in the fits headers of the reduced images. This agrees to within less than 1% with the pixel scale determined astrometrically during other programs (cf., e.g., Mugrauer et al. 2010).

This relatively simple procedure has the advantage of working locally around Rst 137B, meaning that it only requires an images section of about  $30 \times 30$  pixels around the target. Additionally, it is very robust. In particular, it does not require another well-exposed point source in the same image or additional calibration exposures, which are often not available for our images. Naturally, the PSF of an adaptive optics system like NACO is neither strictly constant across the field of view nor a Gaussian (see, e.g., Clénet et al. 2008). However, as the analysis of Clénet et al. also shows, the core of the NACO PSF is usually well behaved. Consequently, it can be well approximated by a Gaussian centered on its maximum. We checked this fact as illustrated in Fig. 3, which shows cuts through one of our NACO images and the corresponding 2-Gaussian model for comparison.

As Fig. 3 shows, our Gaussian model closely fits the PSF down to a level of about 20% of the maximum. It also illustrates that the background,  $a_0$ , in our model does not represent the true background level of the image, because our model does not account for the asymmetric, non-Gaussian tail of the PSF. To focus the fit on the PSF core, we supplied our Levenberg-Marquart routine with weights proportional to the square of each data point. While this procedure is clearly ad hoc, we made sure that details of the weighting function did not significantly influence our determined positions of the Rst 137B components.

To estimate the precision of our coordinate measurement, we applied the fitting procedure described above to the unprocessed NACO images, that is, to all individual exposures of the dithering patterns that were combined by the pipeline reduction. With the exception of the images taken around 25 August 2008, when the closest encounter was observed, the standard deviations of the component distances determined from the individual frames was about 3.0 mas. For the measurements on 25 August 2008, the standard deviation of the component distance is 2.6 mas when considering two out of 17 individual images as outliers. The  $K$ s-band contrast determined for them is unphysical and the distance deviates by more than a factor of two from the determined mean of 19 mas. Hence, we adopted 3.0 mas as the standard error in our orbit modeling for all but the August 2008 measurement, which we treat as an upper limit without uncertainty, see the discussion below.

Alongside the position measurements, Table 2 presents our flux-ratio measurements. Neglecting the measurement of 2 March 2004 because it was taken with the NB 2.17 filter, and the measurements on 28 November 2005 and 25 August 2008 because we consider them outliers, we derive a mean flux ratio of  $0.76 \pm 0.02$  in the  $K$ s band. This agrees with the value of  $0.78 \pm 0.01$  given by Janson et al. (2007), and we regard this a sanity check of our simplified PSF model.

Again, the 25 August 2008 image represents an exception. As shown in Fig. 4, the PSFs of the two components, separated by little more than one CCD pixel, overlap widely. By construction, our fitting approach neglects the PSF tails, which could supply additional position information. Consequently, we cannot separate the two components for this image as precisely as for the other images. Here our fitting algorithm yields a flux contrast of  $(1/2.1 = 0.48)$ , which probably arises because the fainter component was modeled as too faint. As a result, the fit needs to move the fainter component to a larger distance to model the elongation of the image of Rst 137B that is clearly visible in Fig. 4. Thus, our determined distance probably systematically exceeds the true value, and we interpret it as an upper limit of 19.0 mas for the distance of the components on this date.

#### 3.2. Determining the orbit

Using the relative positions given in Table 2, estimates and credibility intervals for the orbital elements of the Rst 137B system can be derived. Following Roy (1978), we parameterized the orbit using the orbital inclination,  $i$ , the semimajor axis,  $a$ , the time of periastron passage,  $\tau$  (measured relative to 2004.0 in our case), the eccentricity,  $e$ , the orbital period,  $P$ , the longitude of periastron,  $\omega$ , and the longitude of the ascending node,  $\Omega$ . The orbital inclination,  $i$ , is the angle between the orbital and the sky plane and the direction of their intersection line is described by  $\Omega$ . Finally,  $\omega$  specifies the orientation of the orbit within the orbital plane.<sup>2</sup>

We adopted 3.0 mas as the standard error on the individual measurements of the distance between Rst 137Ba and Rst 137Bb and 19.0 mas as an upper limit on the distance at 2008.65. Summarizing all orbital elements in the vector  $E$  and denoting the orbital model projected onto the celestial plane evaluated at time  $t$  by  $K(E, t)$ , the resulting posterior probability density

<sup>2</sup> A useful illustration of the orbital elements can be found at [ugastro.berkeley.edu/infrared10/adaptiveoptics/binary\\_orbit.pdf](http://ugastro.berkeley.edu/infrared10/adaptiveoptics/binary_orbit.pdf)

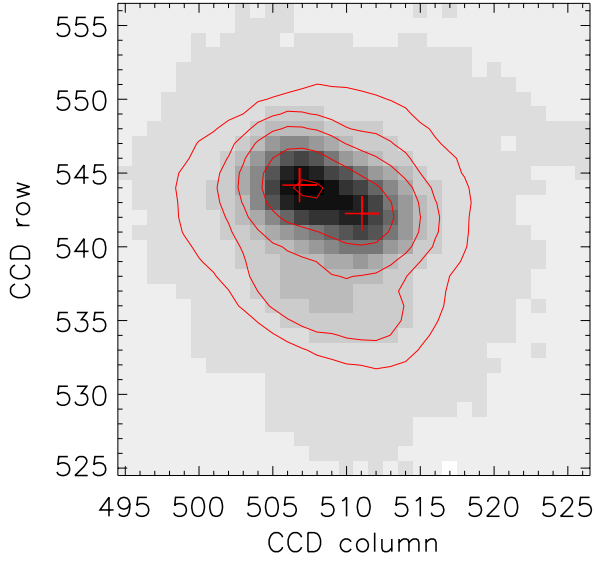


**Fig. 2.** Two components of AB Dor near apastron on 1 January 2009, observed with VLT/NACO. North is up, east is left; the scale is 0.13 arcsec/pix. The contours indicate 95, 50, 20, 10, and 5% of the maximum flux. The crosses indicate the positions of the two components as determined by our 2D Gaussian model. The downward blob, most pronounced in the 10%–contour, is due to a pronouncedly asymmetric wing of the PSF of this image.

becomes

$$p(\mathbf{E}|D) \sim \prod_{i, t_i \neq 2008.65} \exp\left(-\frac{|K(\mathbf{E}, t_i) - pos_i|^2}{2 \cdot (3.0 \text{ mas})^2}\right) \times H(19.0 \text{ mas} - |K(\mathbf{E}, 2008.65)|). \quad (2)$$

Here,  $pos_i$  indicates the  $i$ th position measurement,  $H$  is Heaviside’s step function,  $|K(\mathbf{E}, 2008.65)|$  the model prediction for the distance of the components at 2008.65, and  $D$  denotes the data. We specified uniform priors for all parameters to express our lack of prior knowledge of the orbital solution and used the Markov chain Monte Carlo (MCMC) technique to draw samples from the posterior-probability distribution.

The relative radial velocity between the primary and secondary component determined spectroscopically from our UVES observations at 2009.90 (see Sect. 4.2) represents another piece of information that can be incorporated into the posterior. However, we found from corresponding Markov chains that the RV information only marginally alters the resulting orbital parameters. Table 3 shows the expectation values along with the 95% highest probability density (HPD) credibility interval for all orbital parameters. For comparison, the final column incorporates the 2009.90 RV measurement,  $(8.5 \pm 3) \text{ km s}^{-1}$ , while the middle column does not. An orbit solution based on these expectation values is shown in Fig. 5. The figure shows that our orbit model agrees with all our NACO position measurements within the estimated uncertainties.

The orbital period of 0.988 a or 361 days is close to one year; already Close et al. (2007), based on fewer measurements, estimated it to be “close to 11 months”. This causes the uneven sampling of the orbit by the available observations, which have been scheduled to optimize target visibility. Nonetheless, the repeated observations during different orbits allow determining the period  $P$  to within less than  $\pm 1\%$ , corresponding to  $\approx 2.5$  days. From the 2008.65 measurement, the observations allow constraining the sky-projected distance close to periastron. This, in turn, helps to constrain the semimajor axis of the orbit with a

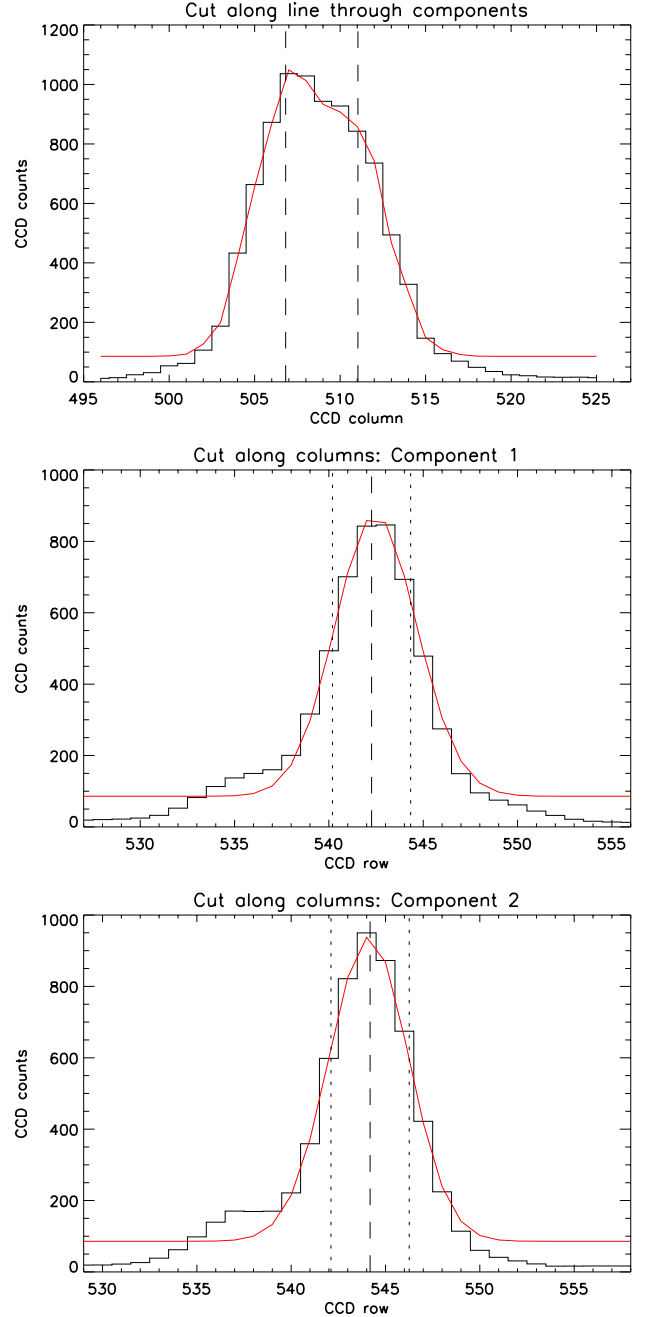


**Fig. 3.** Cuts through the image shown in Fig. 2. The vertical cuts of the two lower panels clearly show the asymmetric PSF wing; they also illustrate that our Gaussian PSF model, shown as the continuous graphs, reliably fits the PSF core in spite of this asymmetry.

relative error of about 20%, which dominates the error of our dynamical mass estimate presented below. Only the parameters  $\omega$ ,  $\Omega$ , and  $e$ , related to the orientation of the orbit, are strongly correlated with Pearson correlation coefficients between 0.75 and 0.9.

The 2008.65 measurement is a critical point for our orbit determination since it contains the only direct information about the orbit close to periastron. We have checked the influence of this measurement on the determined parameters from Markov chains with a posterior not including the 2008.65 measurement. First of all, the critical point suppresses orbits with relatively small semimajor axes and correspondingly higher eccentricities. The resulting expectation value and 95% HPD interval of

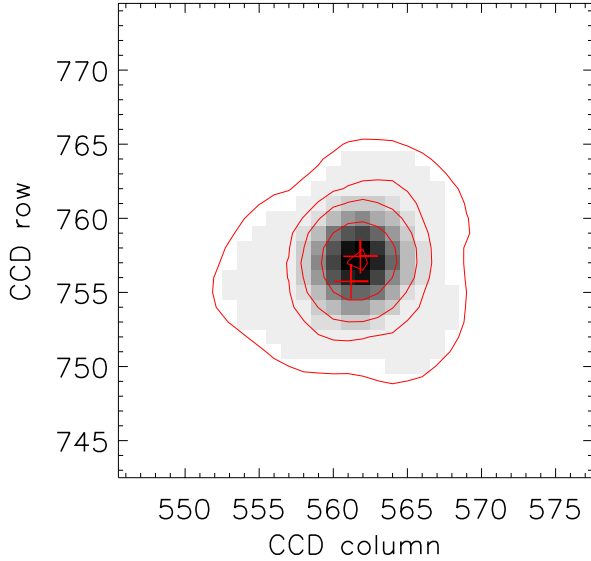


**Fig. 4.** The two components of AB Dor at their closest observed approach on 25 August 2008 (2008.65). See Fig. 2 for annotations. From this observation we determine an upper limit of  $19 \pm 3$  mas for the smallest observed distance of the system, see Sect. 3.1 for a discussion.

the semimajor axis are 48 (38 – 49) for the case excluding the RV measurement at 2009.90.

### 3.3. The combined mass of Rst 137B

The orbital solution for Rst 137Bab discussed in Sect. 3.2 allows estimating the combined dynamical mass ( $m_a + m_b$ ) of the system. To obtain the distribution of the dynamical mass, we used the Markov chains presented in Sect. 3.2, which convert orbital parameters into mass by Kepler’s third law

$$(m_a + m_b) [M_\odot] = \frac{a^3 [\text{AU}]}{P^2 [\text{yr}]} \quad (3)$$

In the calculation, we adopted AB Dor A’s parallax of  $15.17 \pm 0.13$  pc for Rst 137B (van Leeuwen 2007).

Our analysis yields an expectation value of  $0.69$  ( $0.45$ – $0.71$ )  $M_\odot$  for the total dynamical mass of Rst 137B, where the 68% HPD is given in parenthesis. The corresponding 95% HPD interval for the system mass is  $0.35$ – $1.07$   $M_\odot$ . These values were determined including our distance measurement close to periastron at 2008.65, but excluding our RV measurement at 2009.90. The influence of this RV measurement on the mass estimate is relatively small. Furthermore, we do not have a reliable handle on its uncertainty because it depends on the template spectrum used for the measurement. As discussed in more detail Sect. 5.1, this dynamical mass estimate is marginally larger than the mass estimated by Janson et al. (2007). The resulting posterior mass distribution is shown in Fig. 6. It contains a tail of high masses, which are not at all compatible with the brightness of the system components and are, therefore, unphysical. To evaluate the influence of this tail on the overall mass estimate, we produced an additional Markov chain including an upper limit of  $1.0$   $M_\odot$  as a prior on the dynamical mass. The resulting expectation value is  $0.61$  ( $0.46$ – $0.68$ )  $M_\odot$ , which is only slightly lower than the value determined without that prior.

As discussed in Sect. 3.2, the distance measurement close to periastron at 2008.65 has a significant influence on the

**Table 3.** MCMC derived orbital elements, the given uncertainties are 95% highest probability density credibility intervals.

Parameter	(No RV information)	(Incl. RV information)
$a$ [mas]	$56.8^{+13.2}_{-10.0}$	$56.1^{+11.0}_{-9.4}$
$e$	$0.57^{+0.25}_{-0.23}$	$0.55^{+0.23}_{-0.22}$
$i$ [°]	$120.1^{+9.2}_{-9.6}$	$119.8^{+9.4}_{-9.1}$
$P$ [yr]	$0.9884^{+0.0076}_{-0.0083}$	$0.9884^{+0.0072}_{-0.0074}$
$\tau$ [yr]	$1.66^{+0.05}_{-0.05}$	$1.66^{+0.05}_{-0.05}$
$\omega$ [°]	$58^{+24}_{-24}$	$57^{+23}_{-23}$
$\Omega$ [°]	$183^{+22}_{-19}$	$182^{+20}_{-18}$

**Notes.** See Sect. 3.2 for details.

determined orbital parameters. The resulting lower expectation value of the semimajor axis reduces the mass estimate to  $0.44$  ( $0.21$ – $0.41$ )  $M_\odot$ , with 68% HPD in parenthesis. The corresponding probability density of the mass is also shown in Fig. 6. See Sect. 5.1 for the in-depth discussion.

### 3.4. Interpreting the Ks-band contrast

The Ks-band brightness ratio of  $0.76 \pm 0.02$  corresponds to a brightness difference of 0.3 mag. Assuming that the components of Rst 137B are coeval, evolutionary tracks can be used to translate this result into estimates of mass, radius, and effective temperature differences.

Janson et al. (2007) give an upper limit of  $0.4$   $M_\odot$  for the total mass of the Rst 137B system, for which they estimate an age of 50–150 Myr. For different primary component masses between  $0.1$  and  $0.5$   $M_\odot$  and a series of assumed system ages in the range specified by Janson et al., we estimated the corresponding properties of the secondary component, based on the evolutionary tracks of Baraffe et al. (1998) and the Ks-band brightness difference of 0.3 mag. We consider the latter differential measurement a robust photometric information.

With this approach, we find that the secondary should be 30–80 K cooler and between  $0.02$  and  $0.08$   $M_\odot$  less massive than the primary component, see Fig. 7 for the mass difference. Taken from the Baraffe-models accordingly, the radius of the secondary is  $0.92$ – $0.95$  times smaller than that of the primary component. These differences depend more strongly on the primary mass than on the system’s age, except for a very massive primary.

We conclude that independent of the exact age of the system and the primary mass, both components are similar in their properties, with the secondary approximately 20% less massive than the primary and the effective temperature not farther off than 80 K.

## 4. Modeling the stellar spectra

To study the properties of the Rst 137B system, we modeled the spectrum of Rst 137B using first the spectrum of YZ CMi as a stellar template and second, PHOENIX model spectra. While the stellar template is well suited for obtaining estimates of the radial and rotational velocities of the components, the model spectra allow estimating the effective temperature on an absolute scale.

The two UVES spectra taken around 2:00 UT exhibit stronger chromospheric emission lines than the later spectra taken at about 8:20 UT (see Sect. 4.3), indicating a change in activity. For the following analysis, we combined the two

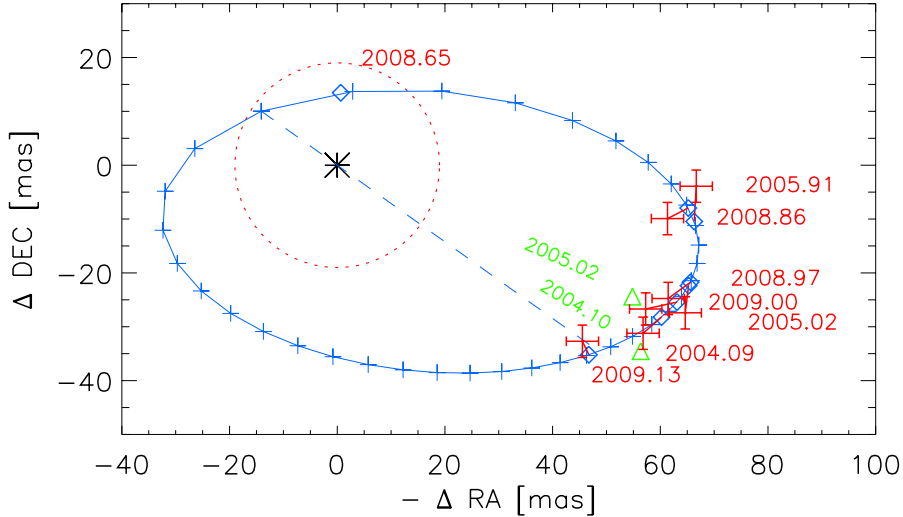


**Fig. 5.** Orbit of AB Dor B projected on the sky as determined by our MCMC model (north up, east left). Red error bars represent positions measured in the NACO images, each linked to a blue diamond that indicates the corresponding position of our orbit model. The standard deviation of the measured distances between the two components is about 3.0 mas. The upper limit for the distance at 2008.65 is indicated by the dashed circle, also determined with an uncertainty of about 3.0 mas. Plus symbols mark approximately 10-day intervals on the orbit, and the dashed line connects its periastron and apastron. The two previously published positions are indicated by green triangles; they were not used for our model. See Sect. 3.2 for details.

low-activity spectra observed around 8:20 UT. Providing our best proxy of the quiescent stellar atmosphere, we only used this spectrum in our modeling. We caution, however, that even low activity levels can influence the determined effective temperature for low-mass objects (e.g., Stassun et al. 2012). Although the spectrum must be composed of two individual components, they are not clearly separated in the data. This confirms that the components are not only similar in effective temperature, but also in radial and rotational velocity.

In applying rotational broadening to the theoretical or stellar template spectrum, we assume linear limb-darkening with a limb-darkening coefficient fixed at a value of 0.6 for both components (Claret 2004).

#### 4.1. Spectral modeling based on an observed template

We compared the spectrum of Rst 137B with spectra of AD Leo, YZ CMi, and CN Leo, which show effective temperatures of 3410 K, 3300 K, and 3150 K according to Reiners & Basri (2007). By visual inspection, we determined that YZ CMi provides the best match for the spectrum of Rst 137B.

To compare the spectra quantitatively, we obtained 50 UVES exposures of YZ CMi taken on March 9 and 10, 2009, in the frame of program 082.D-0953(A) from the ESO data archive. We reduced these data analogously to those of Rst 137B (see Sect. 2.1). Although both the spectra of Rst 137B and those of YZ CMi were obtained in dichroic-2 mode, the setting applied to observe the latter provides a redder wavelength coverage. While the slit width used in our observations was 0.8'', that used to observe YZ CMi was 1''. Therefore, the resolving power in our observations is about 10% higher. To construct a template spectrum of YZ CMi, we co-added the individual spectra.

In a first step, we fitted the template spectrum of YZ CMi to our quiescent spectra of Rst 137B. We concentrated on the 6600–6800 Å and 7040–7165 Å bands, which both show strong molecular band heads and weak telluric contamination. In the fit, we adapted the rotational velocity, the radial velocity shift, and the normalization. While we find a constant normalization to be

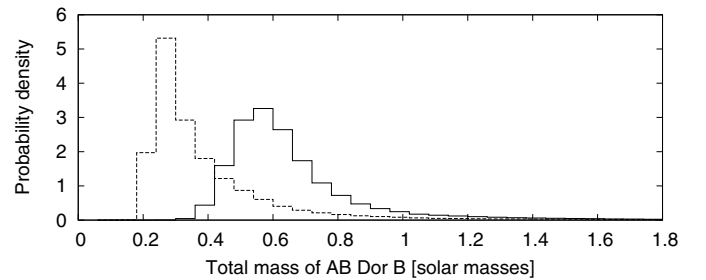


**Fig. 6.** Probability density for the combined mass of Rst 137B, resulting from the MCMC orbit determination: The solid graph is determined including the measurement at 2008.65, while the dashed distribution is obtained without it.

adequate in the 7040–7165 Å band, the residuals show a clear linear trend in the 6600–6800 Å band, which we accounted for by allowing a gradient in the normalization. The results are summarized in Table 4. Note that we added 5 km s<sup>-1</sup> to the actual fit result for the rotational broadening to account for the rotation of YZ CMi (Reiners 2007). The radial velocities were corrected for barycentric motion and the radial velocity of YZ CMi, for which we adopted a value of 26.6 km s<sup>-1</sup> (Morin et al. 2008). The formal 90% confidence interval on the radial and rotation velocities has a width of about 0.2 km s<sup>-1</sup>. However, given the slightly different spectral resolutions of the target and template spectra and some uncertainty of the adopted  $v \sin(i)$  of YZ CMi, we estimate that the error margin in the rotational velocities amounts to a few kilometers per second.

In a second step, we extended our spectral model to account for the binary nature of Rst 137B. In Sect. 3.4, we combined the *K*s-band contrast and evolutionary tracks to derive relations between the masses, effective temperatures, and radii of Rst 137Ba and Rst 137Bb. As both components show similar properties, we used the spectrum of YZ CMi to represent either component and fix the relative flux to the square of the alleged radius ratio. We considered independent radial and rotational velocities for both spectral components. In Table 4 we give the

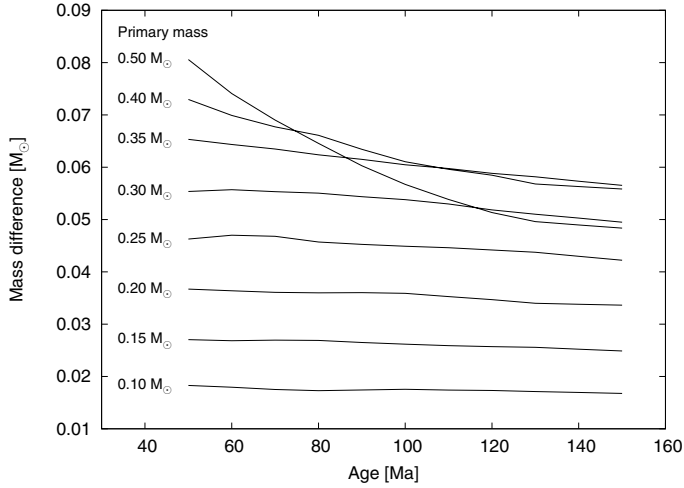


**Fig. 7.** Estimated mass difference of Rst 137Ba and Rst 137Bb as a function of age and primary mass, see text for details.

**Table 4.** Radial and rotation velocity of Rst 137B derived from the YZ CMi template fit assuming a single and a binary star.

	Single model	
	6600–6800 Å	7040–7165 Å
RV [km s <sup>-1</sup> ]	32.1	30.8
$v \sin(i)$ [km s <sup>-1</sup> ]	34.9	37.1
$\chi^2/\text{d.o.f.}$	24 132/11 357	33 553/7097
	Binary model	
RV <sub>a</sub> [km s <sup>-1</sup> ]	26.9 ± 0.3	25.7 ± 0.2
RV <sub>b</sub> [km s <sup>-1</sup> ]	35.1 ± 0.3	34.8 ± 0.2
$v \sin(i)_a$ [km s <sup>-1</sup> ]	40.0 ± 0.4	43.4 ± 0.4
$v \sin(i)_b$ [km s <sup>-1</sup> ]	31.2 ± 0.3	32.0 ± 0.1
$\chi^2/\text{d.o.f.}$	22 143/11 355	28 468/7095

results obtained from fitting the two spectral bands; the subscript *a* refers to the brighter (i.e., larger) component, whereas *b* refers to the smaller component. We caution, however, that the components are indistinguishable in the modeling, meaning that the brighter and fainter component may be interchanged without significantly altering the fit quality. The error margins refer to 95% credibility intervals. Employing an F-test, we find that the two-component solution provides a significantly better fit in both spectral bands.

To roughly estimate the rotation periods of the two stellar components of Rst 137B, we used 30 km s<sup>-1</sup> as a lower limit to their equatorial rotation velocity and 0.52 solar radii as an upper limit of their size. The latter value results from the evolution models (Baraffe et al. 1998), assuming an age of 50 Myr and a mass of 0.45 solar masses – both truly conservative limits in the context of our results. Using  $P = 2\pi \cdot R_*/v_{\text{eq}}$ , we find an upper limit of 0.88 d for the rotation period.

The center-of-mass radial velocity shift of Rst 137B amounts to about 31 km s<sup>-1</sup>. Using the currently observed separation of ≈140 AU between the AB Dor A and Rst 137B component as very rough estimate of the semimajor axis, and furthermore assuming a total of one solar mass in the system, Kepler’s third law yields an orbital period of ≈1500 yr. The orbital velocity would then be on the order of a few kilometers per second, which is compatible with the observations and a radial velocity of 28.5 ± 0.6 km s<sup>-1</sup> for AB Dor (Luhman et al. 2005).

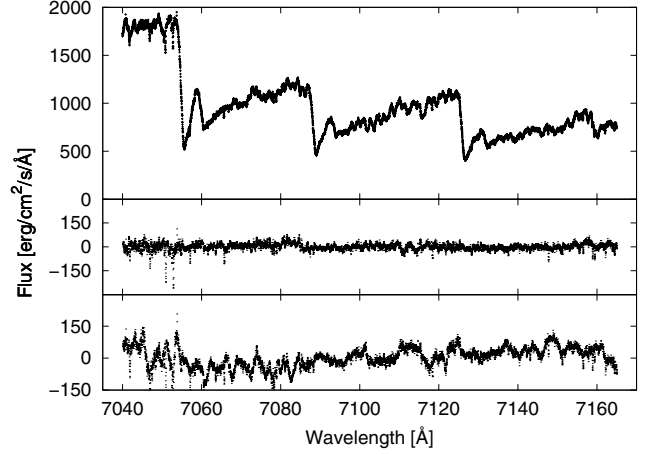


**Fig. 8.** Upper panel: one section of our spectrum of Rst 137B used for the spectral modeling. Middle panel: residuals of our best fit achieved with the YZ CMi template. Lower panel: same as above for the PHOENIX template spectrum.

#### 4.2. Spectral modeling based on PHOENIX spectra

Our modeling is based on PHOENIX ACES model spectra (Hauschildt et al. 1999)<sup>3</sup>. Our spectral grid ranges from 2800 to 3800 K in effective temperature in steps of 100 K;  $\log(g)$  was fixed at a value of 5.0, appropriate for M-dwarfs with ages around 100 Myr (cf., e.g., Baraffe et al. 1998). To obtain model spectra with intermediate temperatures, we interpolated linearly between the grid spectra.

We note that unlike the stellar template, the model spectra fail to reproduce many detailed features of the observed spectrum and, therefore the fit quality remains limited. In our modeling, we concentrated on the 7040–7165 Å band, which shows several molecular band heads and weak telluric contamination (see Fig. 8).

As discussed in Sect. 3.4, the *K*s-band observations can be used to constrain the temperature difference between Rst 137B a and Rst 137B b to within a few 10 K. In a series of test runs, we verified that this temperature difference can only be determined to within a few 100 K from the spectra alone. Hence, in the following we used a model composed of two spectra with a fixed temperature difference of 60 K, which is representative of our results in Sect. 3.4. The same problem arises for the relative contribution of the primary and secondary in the model, which we parameterized by the radius ratio. We fixed this ratio at a value of 0.935, which again is representative of our estimates based on the *K*s-band contrast and the evolutionary models of Baraffe et al. (1998). For both spectral components, we considered individual radial-velocity shifts and projected rotational velocities.

In Table 5, we list estimates of the component parameters resulting from our spectral modeling. To estimate their uncertainties, also accounting for mismatches between the observed spectrum and the templates, we repeated the MCMC sampling using three wavelength subintervals: 7040–7080 Å, 7080–7140 Å, and 7120–7165 Å. The resulting lowest and highest values are given as the limits of the ranges in Table 5.

The rotational and radial velocities derived using the PHOENIX models are compatible with those obtained using YZ CMi as a template (note that the components are

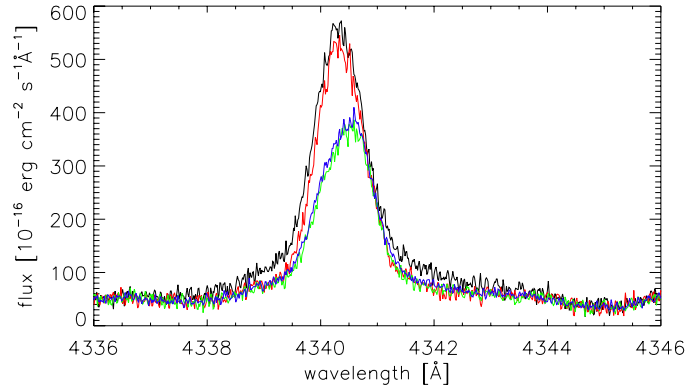
<sup>3</sup> Available at

<ftp://ftp.hs.uni-hamburg.de/pub/outgoing/phoenix/PHOENIX-ACES-2009/AGS/Cond/Z-0.0>

**Table 5.** Spectroscopically determined parameters of Rst 137Ba and Rst 137Bb, using PHOENIX spectra and adopting  $\log(g) = 5.0$ .

$T_a$ [K]	3260–3360
$T_b$ [K]	3200–3300
$v_{r,a}$ [km s <sup>-1</sup> ]	39–40
$v_{r,b}$ [km s <sup>-1</sup> ]	22–24
$v \sin(i)_a$ [km s <sup>-1</sup> ]	30–35
$v \sin(i)_b$ [km s <sup>-1</sup> ]	36–40

**Notes.** The difference in effective temperature between the components of  $T_a - T_b = 60$  K is fixed in our model, see Sect. 3.4 for details.


**Fig. 9.**  $H\gamma$  spectra of Rst 137B taken at 01:56 UT (black), 02:03 UT (red), 08:20 UT (green), and 08:24 UT (blue).

interchanged). Our results for the effective temperature are compatible with those given by Janson et al. (2007), who derive a range of 3145–3305 K for the primary component. Per constructionem, we obtain a temperature of 3140–3270 K for the secondary, which also complies with the results of Janson et al. (2007).

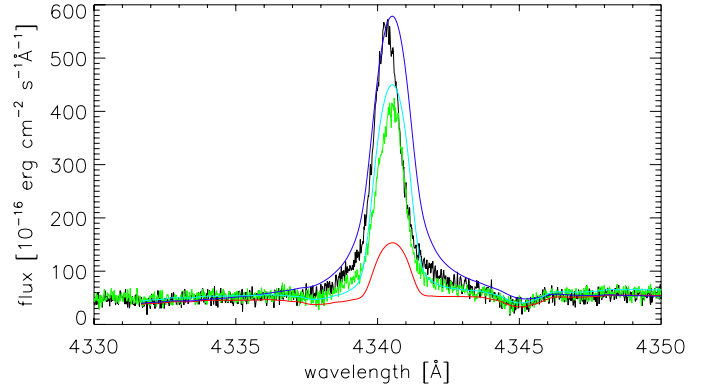
To check the influence of  $\log(g)$  on the temperature, fixed at 5.0 in our modeling, we also adopted values of 4.5 and 4.0 and repeated the fit. We find that lower surface gravities lead to higher effective temperature estimates. For example, we obtain an effective temperature of 3339 K with  $\log(g) = 4.5$  and 3440 K with  $\log(g) = 4$  for the primary in the 7040–7165 Å band.

#### 4.3. Chromospheric activity

As outlined in Sect. 2.1 we observed two pairs of spectra of Rst 137B about six hours apart. As Fig. 9 shows exemplarily for the  $H\gamma$  line, the chromospheric emission changed considerably during that time. Furthermore, there are small changes during the few minutes covered by the first pair of spectra, most pronounced in the line wings. We interpret these changes as indications of a small flare observed some unknown time after its impulsive phase and investigate this hypothesis below.

We detect the Balmer lines in emission down to 3721 Å, that is, to the blue limit of our wavelength range. Furthermore, we detect emission in He ( $D_3$ , He I at 4471 and 6678 Å), Ca II H and K and Na I D (as absorption lines with an emission core), Mg I weakly at 3829, 3832, and 3838 Å, Si I weakly at 3905 Å, and Ca I even weaker at 4226 Å (absorption with emission core). The lines described as weak were only detected in spectra 1 and 2.

All Balmer lines share the same behavior in the sense that their cores decrease markedly in amplitude between spectra 2 and 3 and shift blueward during that time. Differences in their


**Fig. 10.** Our Rst 137B spectra around  $H\gamma$  observed at 01:56 (black) and 08:20 (green) on 26 November 2009 compared with spectra of Proxima Centauri taken during a flare peak (dark blue), flare decay (turquoise), and quiescence (red).

shape, for example, concerning their outer wings or broad component, are described below. For  $H\alpha$  we measure a decrease in equivalent width from  $8.0 \pm 0.5$  Å to  $7.0 \pm 0.5$  Å, that is, by about 10%. This EW is measured between 6555 Å and 6570 Å and using the quasi-continuum around these points for normalization. While this choice should include any broad wing emission, it is to some degree arbitrary and dominates the given uncertainty. Fitting a Gaussian to the  $H\alpha$  emission core, which yields a reasonably good model, we find radial velocities of  $23.3 \pm 2.5$  km s<sup>-1</sup> (spectrum 1) and  $29.3 \pm 2.5$  km s<sup>-1</sup> (spectrum 4). Here, the uncertainty is estimated from deficits of the Gaussian model.

Only the Balmer lines (and weakly Ca II H and K) in spectrum 1 exhibit weak broad components in addition to a narrow main component. This broad component is significantly redshifted in  $H\alpha$ , while it is only marginally shifted in the other Balmer lines. Such broad line wings, redshifted relative to the narrow main component, have previously been observed in M dwarfs, but only during flares (Crespo-Chacón et al. 2006; Fuhrmeister et al. 2008, 2011). Vilhu et al. (1991) also found broad line wings in  $H\alpha$  for AB Dor B in spectra taken 1987, with more flux on the red wing after subtraction of an M3 standard. This suggests that Vilhu et al. may indeed also have observed a flare on AB Dor B. Unfortunately, they only present a single spectrum and do not give the timespan during which that spectrum was taken. However, the  $H\alpha$  profile in their spectrum (their Fig. 5) has nearly the same amplitude above the surrounding quasi-continuum as found in our spectra 1 and 2, which exceeds the quasi-continuum by factors of about 5.

To additionally assess the activity level of Rst 137B, we compared our Balmer line observations with spectra of the moderately active dM5.5 star Proxima Centauri, which we observed during a flare on 2009 March 14 (Fuhrmeister et al. 2011). To this end, the spectra of Proxima Centauri were scaled to match the quasi-continuum of Rst 137B and broadened to 50 km s<sup>-1</sup> rotational velocity. These spectra of Proxima Centauri were taken subsequently and had an exposure time of 1800 s each, with one spectrum covering the flare peak. We took the spectra directly before and after the peak as proxies for the quiescence and flare decay, respectively. As Fig. 10 illustrates, the Balmer line emission of Rst 137B during our observations quite closely matches the behavior of Proxima Centauri during a flare, albeit with a slightly different timing.

From these indications, we argue that we observed the decay of a small flare on AB Dor B in our optical spectra. The small decline of the chromospheric fluxes in the eight minutes between these spectra indicates that our spectrum probably does not cover the impulsive phase of this flare. Compared with ours, the optical spectra of Vilhu et al. (1991) suggest that they also happened to cover a flare, which would mean that their line flux measurements of Rst 137B do not represent a quiescent state of its components. Our lowest measured equivalent width in H $\alpha$  is about 30% below their measurement ( $10 \pm 0.5 \text{ \AA}$ ). However, it should be kept in mind when comparing these values that we do not know their choice of quasi-continuum points and measurement interval.

#### 4.4. Evolution of X-ray and radio emission

During our 58 ksec *XMM-Newton* exposure we detected  $1369 \pm 37$  photons in the 0.2–3.0 keV band, which we attribute to Rst 137B, using the 2 arcsec-radius extraction region shown in Fig. 1. The given formal error is exceeded by the uncertainty of the contamination signal in the chosen aperture for Rst 137B, see Sect. 2.3, and we estimate the true uncertainty to roughly 100 counts. This translates into an average X-ray luminosity of  $L_X = 8 \times 10^{28} \text{ erg s}^{-1}$  in the 0.2–5.0 keV band with an uncertainty of about 10%.

In Fig. 11 we show our X-ray and radio light curves. While the upper panel combines the radio light curves of AB Dor A and Rst 137B, the panels below show them separately for AB Dor A and Rst 137B. While AB Dor A is clearly variable in both bands, Rst 137B shows no significant variations in our radio light-curve.

The shown X-ray signal of Rst 137B varies by about a factor of three, peak-to-peak. It must be kept in mind that the signal of Rst 137B in the MOS1-detector of *XMM-Newton* can only be extracted after subtracting an estimate of the strong contamination by AB Dor A (see Sect. 2.3 and Fig. 1). Our estimate of this contamination is shown in the lower panel of Fig. 11.

The chromospheric flare starting before 2:00 UT on 26 November (26 h in Fig. 11) is probably not covered by the radio light-curve. Our estimated X-ray flux of Rst 137B shows an increase by about a factor of two around this time. However, given the strong contamination signal by AB Dor A and its significant variations, we summarize that we do not see a significant X-ray signature in Rst 137B associated with its presumed chromospheric flare.

## 5. Summary and discussion

As first discovered by Close et al. (2005), Rst 137B (=AB Dor B) consists of two M-dwarfs of slightly different mass: Rst 137Ba and Rst 137Bb. While its membership in the AB Dor system motivates an intensive study, Rst 137B otherwise appears as a very normal young M-dwarf binary: about 30% of all M dwarf primaries are in binary systems, and separations of up to a few AU appear to be most frequent (Fischer & Marcy 1992).

The fast rotation of both components of Rst 137B ( $P_{\text{rot}} \lesssim 0.88 \text{ d}$ , cf. Sect. 4.2) is common for stars in the relevant mass range for ages at least up to the Hyades age ( $\approx 625 \text{ Myr}$ , Perryman et al. 1998), see Fig. 4 of Reiners & Mohanty (2012). Furthermore, the binarity of Rst 137B may well have influenced the rotation history of its components. Hence, the fast rotation does not place a relevant upper limit on the age of Rst 137B.

The eccentric orbit of Rst 137B (see Table 3) does not place a significant upper limit on its age either: already for systems

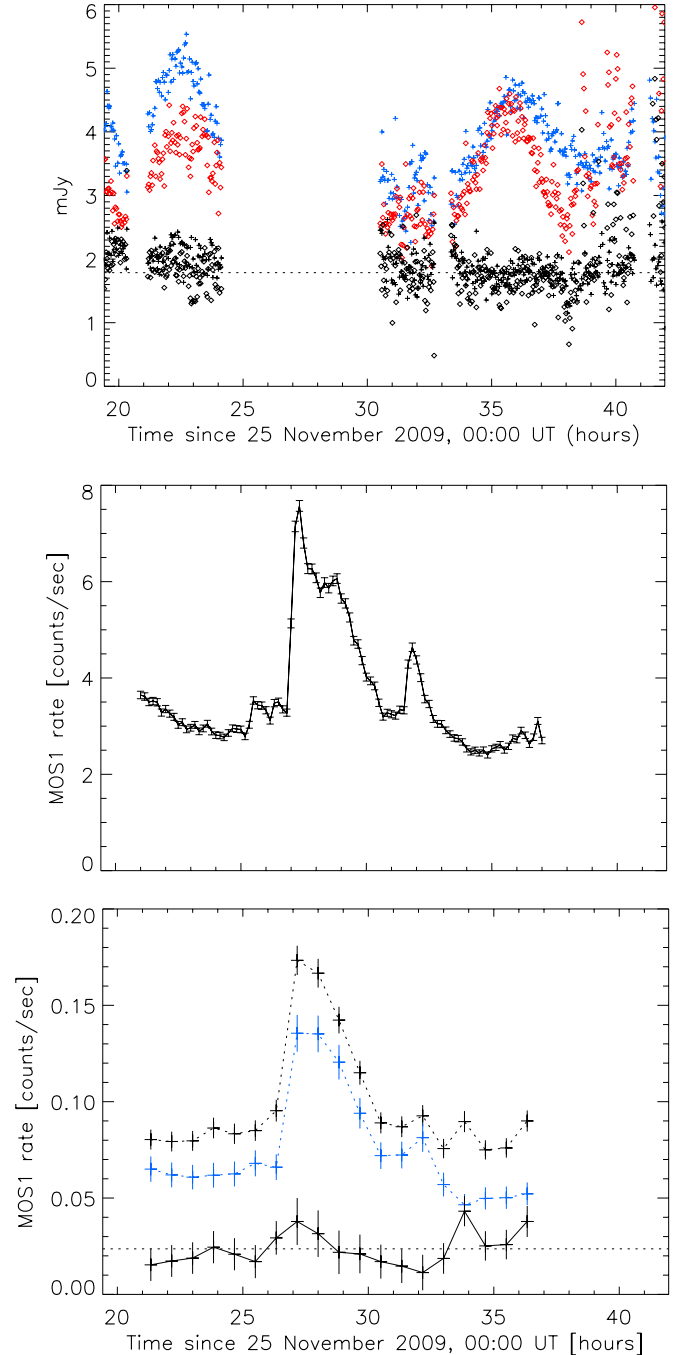


**Fig. 11.** Coronal light curves of AB Dor A and Rst 137B, the components of the latter cannot be separated in any of these data. *Upper panel:* radio flux density of AB Dor A at 5.5 (blue) and 9.0 GHz (red). For Rst 137B the black plus symbols and diamonds represent the two frequencies. The horizontal line denotes the mean flux of Rst 137B at 5.5 GHz. *Middle panel:* soft X-ray count rate of AB Dor A in *XMM-Newton*'s MOS1 detector (0.5–2.0 keV), binned to 600 sec, the bars represent  $1\sigma$  errors. *Lower panel:* same as middle panel for Rst 137B with rates binned to 3000 s. As Fig. 1 illustrates, the signal at the position of Rst 137B (black dotted line) is highly contaminated with photons of AB Dor A. After subtracting our background estimate (blue dotted), we arrive at the continuous black graph which shows the count rate of Rst 137Ba+b. The horizontal dotted line indicates the corresponding mean, see Sect. 2.3 for details.

with orbital periods of a few days circularization operates on timescales of several gigayears (cf., e.g., Mathieu 2005), which makes this clock useless for estimating ages of young stars.

The determination of stellar ages is usually difficult, see [Soderblom \(2010\)](#) for a comprehensive overview. [Soderblom](#) summarizes that only evolutionary isochrones and asteroseismology are reasonably sensitive for individual stars. This leaves us only with the former method for Rst 137B at present, which we apply in the following section. Finally, we summarize the activity properties of Rst 137B found in our analysis.

### 5.1. Mass and age of Rst 137B

As outlined in Sect. 3.3, our orbit model of Rst 137B results in an estimate of  $(m_1 + m_2) = 0.69 (0.45\text{--}0.71) M_\odot$  for the combined mass of Rst 137Ba+b, where the 68% HPD credibility interval is given in parenthesis. If we exclude the only available measurement close to periastron (2008.65), we obtain a significantly lower mass estimate of  $0.44 (0.21\text{--}0.41) M_\odot$ . The  $K$ -band brightness contrast of the components, combined with our spectral modeling, yields an effective temperature estimate of  $3310 \pm 50$  K for the primary, about 60 K lower for the secondary.

Our estimate of the effective temperature is compatible with the values reported by [Janson et al. \(2007\)](#), namely 3145–3305 K and 3080–3240 K. We note that they determine the effective temperatures by an entirely different method, using the estimated spectral type (M3–M5, [Martin & Brandner 1995](#)) and the effective temperature scale of [Kenyon & Hartmann \(1995\)](#).

Furthermore, [Janson et al. \(2007\)](#) derive their mass estimates of  $0.13\text{--}0.2 M_\odot$  for the primary and  $0.11\text{--}0.18 M_\odot$  for the secondary by combining these effective temperatures with estimates of the bolometric luminosity, also using the evolution models of [Baraffe et al. \(1998\)](#). Hence, the mass estimate of [Janson et al. \(2007\)](#) is directly derived from the models of [Baraffe et al. \(1998\)](#). Our dynamical mass estimate favors slightly higher masses for the system components than the values of [Janson et al. \(2007\)](#): it is only marginally compatible with the same evolution models, namely if we assume a system mass of roughly  $0.4 M_\odot$ , which is at the low end of the probability density we derive for the mass (cf. Fig. 6). This assessment makes use of the fact that the mass difference of the Rst 137B components would not exceed  $0.05 M_\odot$  in this scenario, according to the Baraffe models (cf. Fig. 7) When excluding the distance measurement close to periastron, the marginal discrepancy of our mass estimate with the [Baraffe et al. \(1998\)](#) models disappears, as does the deviation from the mass estimate of [Janson et al. \(2007\)](#). However, there is no reason to doubt the validity of this measurement. It appears that more AO observations, more homogeneously distributed along the orbit, are required to settle this question.

We illustrate this situation in Fig. 12, where we combine our spectroscopic information with the IR fluxes measured by [Janson et al. \(2007\)](#) and show evolutionary tracks for the relevant mass range as a function of effective temperature and absolute  $K$ -band magnitude ([Baraffe et al. 1998](#)). These tracks were computed for solar metallicity, which appears to be approximately valid for AB Dor, see, e.g., [Ortega et al. \(2007, their Table 2\)](#). We converted the apparent  $K$ s-magnitudes of [Janson et al. \(2007\)](#) to absolute  $K$ -magnitudes using the distance modulus of  $0.91 \pm 0.02$  mag corresponding to the HIPPARCOS distance of AB Dor. In this way, we assume no significant absorption; given the proximity of AB Dor, this is certainly reasonable concerning interstellar absorption. Note that we used the  $K$ s-band values by [Janson et al. \(2007\)](#) on the  $K$ -band scale of Baraffe’s models. We added the uncertainty of this conversion ( $<0.1$  mag, cf. [Carpenter 2001](#)) to the  $K$ -magnitude errors shown in the figure.

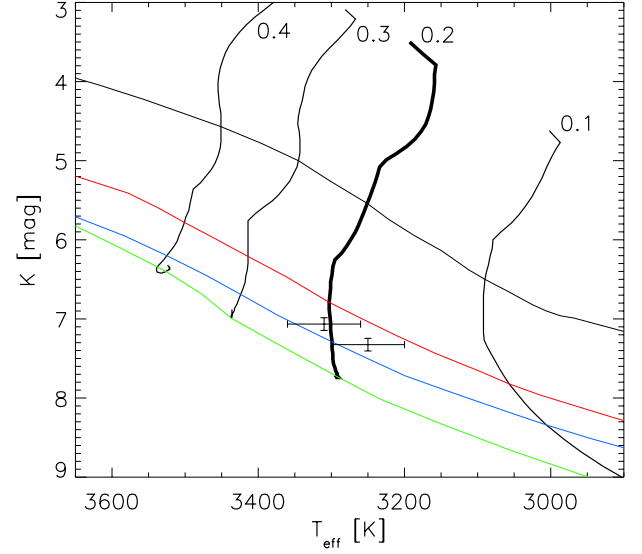


**Fig. 12.** Evolutionary PMS tracks for 0.1 to 0.4 solar masses and solar metallicity, shown as a function of effective temperature and absolute  $K$ -magnitude ([Baraffe et al. 1998](#)). Isochrones are drawn for 10 (black), 50, 100, and 150 Myr (green). The components of Rst 137B are indicated by error bars according to our spectroscopically determined  $T_{\text{eff}}$  and the photometry of [Janson et al. \(2007\)](#), see Sect. 5.1 for details.

As Fig. 12 illustrates, our analysis places Rst 137Ba between the 50 and 100 Myr isochrones of the Baraffe models. We note that Rst 137Ba falls onto the same isochrone by construction of our analysis since we derive the temperature difference based on the same evolution models (cf. Sect. 3.4). We also note that in accord with the Baraffe models, our analysis uses an effective temperature scale based on PHOENIX models.

Our result confirms the age range of 50–100 Myr estimated for Rst 137B by [Janson et al. \(2007\)](#), which is expected since our effective temperature measurement differs only slightly from their values and we used the same evolution models. Our dynamical mass estimate clearly indicates component masses at the upper end of the values of [Janson et al. \(2007\)](#) or even higher, that is,  $\geq 0.4 M_\odot$ . However, the most probable system mass of  $0.65 M_\odot$  predicted by our orbit model cannot be reconciled with the evolution models of [Baraffe et al. \(1998\)](#) and the photometric and spectroscopic models of the system. A more complete sampling of the orbit of Rst 137B is required to resolve this question.

We note that our determined orbital inclination of Rst 137B of  $i_{\text{orbit}} = 120 \pm 9^\circ$  means that the orbit is inclined by about 30 degrees from an edge-on orientation. This orientation can be compared with the tilt of the stellar rotation axis of AB Dor A, determined from Doppler imaging to be  $i_{\text{axial}} \approx 60^\circ$ , which means that it is inclined by about 30 degrees from an equator-on orientation. This value must also be considered uncertain by roughly 10 degrees (cf. [Kuerster et al. 1994](#); [Donati & Collier Cameron 1997](#)). Thus, the projected orientation of the orbit of Rst 137B and the spin axis of AB Dor A appear to approximately coincide. Significant or not, this agrees with a general tendency in multiple systems (see, e.g., [Hale 1994](#); [Watson et al. 2011](#)).

Unfortunately, we do not know the spin orientation of the components of Rst 137B. However, their projected rotational velocities of 30 to 40  $\text{km s}^{-1}$  are high among the  $v \sin i$  observed for mid-M dwarfs ([Jenkins et al. 2009](#)). To roughly estimate the corresponding rotation period, we assumed a star with 0.2 solar masses and an age of 100 Ma. For these values the models of

Baraffe et al. (1998) predict a radius of about 0.12 solar radii. Adopting this radius, a  $v \sin i$  of  $40 \text{ km s}^{-1}$  corresponds to a rotation period of 0.15 days. Again, this is at the lower end of periods observed in this mass range, see Scholz & Eisloffel (2004) and Jeffries et al. (2011), e.g., their Fig. 6. Therefore we argue that the components of Rst 137B are not seen close to pole-on.

## 5.2. Coronal activity: X-rays and radio

Our determined average X-ray luminosity of Rst 137B of  $L_X = 8 \times 10^{28} \text{ erg s}^{-1}$  (0.2–5.0 keV) lies within the range of luminosities previously observed with *XMM-Newton* in this band, namely  $L_X = 4 \times 10^{28} \text{ erg s}^{-1}$  and  $L_X = 2 \times 10^{29} \text{ erg s}^{-1}$ , both observed in 2001. Hence, it is about a factor of two higher than the lowest yet observed X-ray luminosities of Rst 137B, including measurements by other instruments, see also Sect. 1.4. We estimate the systematic uncertainty of the X-ray luminosities of Rst 137B determined with *XMM-Newton* to be up to 30% because of the strong contamination of the signal of Rst 137B by the much brighter AB Dor A in the MOS1 detector, see Sect. 2.3 for details. This should also be kept in mind when interpreting the X-ray variations of Rst 137B by about a factor of three on timescales of hours which we find in our observations in 2009.

In summary, our 2009 X-ray measurements of Rst 137B match previous observations. They confirm that its averaged X-ray luminosity varies by about a factor of five on timescales of years. As a pair of two mid-M dwarfs close to the main sequence, their total luminosity will be on the order of 1/100 of the solar luminosity (e.g., Baraffe et al. 1998), that is,  $10^{31} \text{ erg/s}$ , which places it at the X-ray saturation level for magnetic activity ( $\log L_X/L_{\text{bol}} \sim -3$ ).

Our radio observations at 5.5 GHz and 9.0 GHz reveal no significant variations around a flux density of 2 mJy, which is the same value as observed about 20 years earlier in those bands (cf. Sect. 1.3).

### 5.2.1. Chromospheric activity: optical spectra

We were unable to determine whether one component of Rst 137B dominates the chromospheric emission (a) because the significant chromospheric line profile variations mimic larger radial velocity shifts than our determined difference in RV between Rst 137Ba and b of about  $8 \text{ km s}^{-1}$ . Furthermore; (b) the high projected rotational velocities of both components (see Table 4) also significantly exceed this RV difference. Hence, any chromospheric emission region covering only a small portion of the stellar surface might be rotationally shifted by up to several  $\pm 10 \text{ km s}^{-1}$ . This refutes any attempt to associate a localized emission region, for example, a flare, with one of the components.

Our spectra show the usual chromospheric emission lines found in active M dwarfs. As discussed in Sect. 4.3, we find that probably the chromospheric emission in our spectra is partly due to a weak flare. The  $H\alpha$  spectrum of Rst 137B observed by Vilhu et al. (1991) appears very similar to ours. Hence, their value of  $10 \pm 0.5 \text{ \AA}$  for the  $H\alpha$  EW does presumably not represent the quiescent emission of Rst 137B either, but our measurements only marginally lower this limit by about 30%.

As a consequence, the estimate of Vilhu et al. of  $L_{H\alpha}/L_{\text{bol}}$  of  $2.7\text{--}3.8 \times 10^{-4}$  still appears to be essentially valid. Assuming that the chromospheric activity is indeed shared rather symmetrically between the two components, this would place both Rst 137Ba and b at the saturation limit of chromospheric

emission in terms of  $L_{H\alpha}/L_{\text{bol}}$ . Given their high rotational velocities, this completely agrees with other highly active mid-M dwarfs (see Fig. 9 of Mohanty & Basri 2003; also Fig. 9 of Reiners et al. 2012).

## 6. Conclusions

Rst 137B is reminiscent of other highly active M dwarf binaries, e.g. UV Ceti (e.g. Audard et al. 2003). In contrast to UV Ceti, the activity signatures of the components of Rst 137B could not yet be separated.

We were able for the first time to determine the orbit of the components of Rst 137B, resulting in a dynamical mass estimate. This estimate, given the combined properties of the stars, is marginally consistent with the evolution models of Baraffe et al. (1998), although it suggests that the component masses are larger than predicted by these models. The orbital inclination of Rst 137B appears to be close to the rotation axis orientation of AB Dor A. To confirm this, and to obtain a better constrained mass estimate, a denser sampling of Rst 137B's orbit is required.

*Acknowledgements.* We thank the referee M. Simon for his concise and constructive comments. U.W. acknowledges funding by the Deutsche Forschungsgemeinschaft (DFG) grant Schm 1032/37-1.

## References

- Audard, M., Güdel, M., & Skinner, S. L. 2003, *ApJ*, 589, 983  
 Ballester, P., Modigliani, A., Boitquin, O., et al. 2000, *The Messenger*, 101, 31  
 Baraffe, I., Chabrier, G., Allard, F., & Hauschildt, P. H. 1998, *A&A*, 337, 403  
 Barrado y Navascués, D., Stauffer, J. R., & Jayawardhana, R. 2004, *ApJ*, 614, 386  
 Boccaletti, A., Chauvin, G., Baudoz, P., & Beuzit, J.-L. 2008, *A&A*, 482, 939  
 Carpenter, J. M. 2001, *AJ*, 121, 2851  
 Claret, A. 2004, *A&A*, 428, 1001  
 Clénet, Y., Lidman, C., Gendron, E., et al. 2008, in *SPIE Conf. Ser.*, 7015, 29  
 Close, L. M., Lenzen, R., Guirado, J. C., et al. 2005, *Nature*, 433, 286  
 Close, L. M., Thatte, N., Nielsen, E. L., et al. 2007, *ApJ*, 665, 736  
 Cohen, O., Drake, J. J., Kashyap, V. L., Hussain, G. A. J., & Gombosi, T. I. 2010, *ApJ*, 721, 80  
 Collier Cameron, A., & Foing, B. H. 1997, *The Observatory*, 117, 218  
 Crespo-Chacón, I., Montes, D., García-Alvarez, D., et al. 2006, *A&A*, 452, 987  
 de la Calle, I. 2012, <http://xmm.esac.esa.int>  
 Donati, J.-F., & Collier Cameron, A. 1997, *MNRAS*, 291, 1  
 Fischer, D. A., & Marcy, G. W. 1992, *ApJ*, 396, 178  
 Fuhrmeister, B., Liefke, C., Schmitt, J. H. M. M., & Reiners, A. 2008, *A&A*, 487, 293  
 Fuhrmeister, B., Lalitha, S., Poppenhaeger, K., et al. 2011, *A&A*, 534, A133  
 García-Alvarez, D., Drake, J. J., Kashyap, V. L., Lin, L., & Ball, B. 2008, *ApJ*, 679, 1509  
 Güdel, M. 2004, *A&ARv*, 12, 71  
 Güdel, M., Audard, M., Briggs, K., et al. 2001, *A&A*, 365, L336  
 Guirado, J. C., Reynolds, J. E., Lestrade, J.-F., et al. 1997, *ApJ*, 490, 835  
 Guirado, J. C., Martí-Vidal, I., Marcaide, J. M., et al. 2006, *A&A*, 446, 733  
 Guirado, J. C., Marcaide, J. M., Martí-Vidal, I., et al. 2011, *A&A*, 533, A106  
 Hale, A. 1994, *AJ*, 107, 306  
 Hauschildt, P. H., Allard, F., & Baron, E. 1999, *ApJ*, 512, 377  
 Janson, M., Brandner, W., Lenzen, R., et al. 2007, *A&A*, 462, 615  
 Jeffries, R. D., Jackson, R. J., Briggs, K. R., Evans, P. A., & Pye, J. P. 2011, *MNRAS*, 411, 2099  
 Jenkins, J. S., Ramsey, L. W., Jones, H. R. A., et al. 2009, *ApJ*, 704, 975  
 Kenyon, S. J., & Hartmann, L. 1995, *ApJS*, 101, 117  
 Kuerster, M., Schmitt, J. H. M. M., & Cutispoto, G. 1994, *A&A*, 289, 899  
 Kuerster, M., Schmitt, J. H. M. M., Cutispoto, G., & Dennerl, K. 1997, *A&A*, 320, 831  
 Lalitha, S., Fuhrmeister, B., Wolter, U., et al. 2013, *A&A*, 560, A69  
 Lenzen, R., Hartung, M., Brandner, W., et al. 2003, in *SPIE Conf. Ser.* 4841, eds. M. Iye, & A. F. M. Moorwood, 944  
 Lim, J. 1993, *ApJ*, 405, L33  
 Lim, J., White, S. M., Nelson, G. J., & Benz, A. O. 1994, *ApJ*, 430, 332

- Luhman, K. L. 2012, *ARA&A*, 50, 65  
 Luhman, K. L., Stauffer, J. R., & Mamajek, E. E. 2005, *ApJ*, 628, L69  
 Martin, E. L., & Brandner, W. 1995, *A&A*, 294, 744  
 Mathieu, R. D. 2005, in *Tidal Evolution and Oscillations in Binary Stars*, eds. A. Claret, A. Giménez, & J.-P. Zahn, *ASP Conf. Ser.*, 333, 26  
 Mohanty, S., & Basri, G. 2003, *ApJ*, 583, 451  
 Morin, J., Donati, J.-F., Petit, P., et al. 2008, *MNRAS*, 390, 567  
 Mugrauer, M., Vogt, N., Neuhäuser, R., & Schmidt, T. O. B. 2010, *A&A*, 523, L1  
 Nielsen, E. L., Close, L. M., Guirado, J. C., et al. 2005, *Astron. Nachr.*, 326, 1033  
 Ortega, V. G., Jilinski, E., de La Reza, R., & Bazzanella, B. 2007, *MNRAS*, 377, 441  
 Pakull, M. W. 1981, *A&A*, 104, 33  
 Perryman, M. A. C., Brown, A. G. A., Lebreton, Y., et al. 1998, *A&A*, 331, 81  
 Reiners, A. 2007, *A&A*, 467, 259  
 Reiners, A., & Basri, G. 2007, *ApJ*, 656, 1121  
 Reiners, A., & Mohanty, S. 2012, *ApJ*, 746, 43  
 Reiners, A., Joshi, N., & Goldman, B. 2012, *AJ*, 143, 93  
 Reipurth, B. 2008, *Handbook of Star Forming Regions, Volume II: The Southern Sky*, *ASP Monograph Publications* (Bo Reipurth)  
 Rousset, G., Lacombe, F., Puget, P., et al. 2003, in *SPIE Conf. Ser.*, 4839, eds. P. L. Wizinowich & D. Bonaccini, 140  
 Roy, A. 1978, *Orbital motion*, 4th edn. (Wiley)  
 Rucinski, S. M. 1985, *MNRAS*, 215, 591  
 Sanz-Forcada, J., Maggio, A., & Micela, G. 2003, *A&A*, 408, 1087  
 Scholz, A., & Eislöffel, J. 2004, *A&A*, 421, 259  
 Soderblom, D. R. 2010, *ARA&A*, 48, 581  
 Soderblom, D. R., Laskar, T., Valenti, J. A., Stauffer, J. R., & Rebull, L. M. 2009, *AJ*, 138, 1292  
 Stassun, K. G., Kratter, K. M., Scholz, A., & Dupuy, T. J. 2012, *ApJ*, 756, 47  
 van Leeuwen, F. 2007, *A&A*, 474, 653  
 Vilhu, O., & Linsky, J. L. 1987, *PASP*, 99, 1071  
 Vilhu, O., Gustafsson, B., & Walter, F. M. 1991, *A&A*, 241, 167  
 Watson, C. A., Littlefair, S. P., Diamond, C., et al. 2011, *MNRAS*, 413, L71  
 White, G. L., Jauncey, D. L., Batty, M. J., Peters, W. L., & Gulkis, S. 1988, *PASP*, 100, 825  
 Wichmann, R., Bastian, U., Krautter, J., Jankovics, I., & Rucinski, S. M. 1998, *MNRAS*, 301, L39